Polyfluoroalkyl Chain-Based Assemblies for Biomimetic Catalysis

Ning Liu, Ping Gao, Hai-Yan Lu, Lei Fang, Julien Nicolas, Tâp Ha-Duong, Jiang-Shan Shen

Polyfluoroalkyl Chain-Based Assemblies for Biomimetic Catalysis

Ning Liu,[a] Ping Gao,[b, c] Hai-Yan Lu,[a] Lei Fang,[a] Julien Nicolas,[b] Tâp Ha-Duong,*[c] Jiang-Shan Shen*[a]

[a] N. Liu, H.-Y. Lu, Dr. L. Fang, Prof. J.-S. Shen
College of Materials Science and Engineering
Huaqiao University
Xiamen, 361021, China
E-mail: jsshen@hqu.edu.cn

[b] Dr. P. Gao, Prof. J. Nicolas
Institut Galien Paris-Saclay
Université Paris-Saclay, CNRS
Orsay, 91400, France

[c] Dr. P. Gao, Prof. T. Ha-Duong
BioCIS
Université Paris-Saclay, CNRS
Orsay, 91400, France
E-mail: tap.ha-duong@universite-paris-saclay.fr

Supporting information for this article is given via a link at the end of the document.

Abstract: Amphiphobic fluoroalkyl chains are exploited for creating robust and diverse self-assembled biomimetic catalysts. Long terminal perfluoroalkyl chains (C_nF_{2n+1} with n = 6, 8, and 10) linked with a short perhydroalkyl chains (C_mH_{2m} with m = 2 and 3) were used to synthesize several 1,4,7-triazacyclononane (TACN) derivatives, C_nF_{2n+1}-C_mH_{2m}-TACN. In the presence of an equimolar amount of Zn^{2+} ions that coordinate the TACN moiety and drive the self-assembly into micelle-like aggregates, the critical aggregation concentration of polyfluorinated C_nF_{2n+1}-C_mH_{2m}-TACN·Zn^{2+} was lowered by ~1 order of magnitude compared to the traditional perhyroalkyl counterpart with identical carbon number of alkyl chain. When 2'-hydroxypropyl-4-nitrophenyl phosphate was used as the model phosphate substrate, polyfluorinated C_nF_{2n+1}-C_mH_{2m}-TACN·Zn^{2+} assemblies showed higher affinity and catalytic activity, compared to its perhyroalkyl chain-based counterpart. Coarse-grained molecular dynamic simulations have been introduced to explore the supramolecular assembly of polyfluoroalkyl chains in the presence of Zn^{2+} ions and to better understand their enhanced catalytic activity.

Introduction

Catalysis is crucial for maintaining normal functions of living systems.[1] A considerable number of artificial catalysts have been designed and synthesized to mimic important natural enzymes such as hydrolases, aimed to play a catalytic role in biochemical reactions.[2] Self-assembly is an important process to obtain such mimic enzymes with competitive catalytic activity.[3] Driven by self-assembly, the multiple catalytic units are expected to gather to create multivalent structural systems offering exceptional catalytic performance. In this regard, designing several self-assembled systems to create artificial catalysts to mimic natural hydrolases, such as micelle/vesicle systems,[4] monolayer-protected gold nanoparticles (Au NPs),[5] and coordination polymeric systems,[6] have been well demonstrated, in particular, for the hydrolysis of phosphate esters. For example, a metallated monolayer containing 1,4,7-triazacyclononane (TACN)·Zn^{2+} heads has been anchored on the surface of Au NPs via strong Au-S coordination bond to innovate a multivalent system which exhibited favorable cooperativity in catalysis during the hydrolysis reaction of activated phosphate diesters such as 2'-hydroxypropyl-4-nitrophenyl phosphate (HPNP), always used as a model of RNA. Besides the fact that two TACN·Zn^{2+} heads are required to form a catalytic pocket that captures one HPNP molecule, the cooperativity likely resulted from concentration effects in the reaction loci and from their limited mobility and constrained conformation.[5b] Similar cooperativity was also observed by our group in the case of Ag-SR coordination polymeric structures formed *in situ* upon mixing equimolar amounts of Ag^+ ions and alkyl thiols containing a TACN-moiety for the transphosphorylation reaction of HPNP.[6] In these Ag-SR coordination polymeric systems, Ag^+ ions function as the linking "nodes" to connect thiol groups and bring TACN-moieties in close proximity via strong Ag-S bond. Subsequent addition of equimolar amount of Zn^{2+} ions to complex TACN can activate the system for this catalysis, demonstrating its simplicity. Regarding micelle/vesicle systems, an intriguing example is the recent work reported by the Prins' group.[4a] They demonstrated that the HPNP phosphodiester could not only serve as a substrate, but could also act as a charged counterion to effectively promote the assembly of amphiphilic C_{16}TACN·Zn^{2+}, which carries a long hydrophobic 16-carbon alkyl chain. The promoted assemblies exhibited higher catalytic activity than under the unassembled state (at a concentration below its critical aggregation concentration, CAC). In these cases of micelle/vesicle systems reported by Prins,[4a] könig,[7] Chen,[8] Moss,[9] Bunton,[10] Tonellato,[11] and Menger,[12] respectively. perhydroalkyl chains (H-chains) were used to function as the hydrophobic moiety. A common issue encountered in *H*-chain-based metallomicelles or metallovesicles, featured by a dinuclear catalytic site for the catalysis of phosphodiester substrate, is low cooperativity likely due to a lack of constrained

conformation, a high mobility of *H*-chains, and an intrinsic fragility of these traditional supramolecular assemblies.[9, 13] Therefore, the search for a solution to overcome the poor robustness and cooperativity encountered in traditional micelle or vesicle systems is a crucial topic in the future work.

Compared to H-chains, perfluoroalkyl or highly fluorinated alkyl chains (F-chains) exhibit several advantages: (i) the conformational freedom of F-chains is significantly restricted, (ii) there are significantly lower surface tensions and cohesive energy densities, (iii) the assembled state in water is more "ordered", and (iv) they are considerably more hydrophobic (Scheme 1).[14] For example, Pasquato and Lucarini reported the first example of water soluble gold nanoparticles protected by a monolayer of fluorinated amphiphilic thiols,[15] to demonstrate that the hydrophobicity of fluorocarbons is higher than that of hydrocarbons. On the basis of these favorable features of *F*-chains, we can envision that if *F*-chains are used to create a surfactant-like molecule containing a terminal hydrophilic catalytic head such as TACN·Zn^{2+} for the catalysis of phosphodiester substrates, lower CAC and more compacted assemblies in aqueous solution should be obtained. Thus, a more robust multivalent system will be created. Benefited from these enhanced features, outstanding catalytic activity for the hydrolysis of HPNP is expected in the case of *F*-chain assemblies in aqueous solution, compared to *H*-chains.

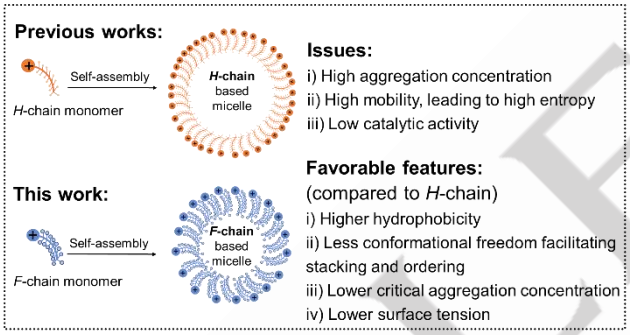

Scheme 1. Comparison of previous work on *H*-chain-based micelle systems and this work on *F*-chain-based micelle systems.

To investigate the aforementioned hypothesis, several TACN derivatives C_nF_{2n+1}-C_mH_{2m}-TACN (n = 6, 8, and 10; m = 2, and 3) containing a long-terminated *F*-chain linked with a short *H*-chain were designed and synthesized (Scheme 2). Upon addition of equimolar amount of Zn^{2+} ions to coordinate the N atoms of the TACN moiety, we found for the C_8F_{17}-C_3H_6-TACN·Zn^{2+} system with 11 carbon atoms in the alkyl chain, that its CAC was ~110 μM. This is not only close to ~95 μM for perhydroalkyl C_{16}-TACN·Zn^{2+} reported by Prins et al., with 16 carbon atoms in the alkyl chain,[4a] but also lower by ~1 order of magnitude than that of its perhydroalkyl chain $C_{11}H_{23}$-TACN·Zn^{2+} counterpart (~1000 μM), highlighting the atom economy of *F*-chain. During catalysis of the hydrolysis reaction of the phosphate model substrate HPNP, under both experimental conditions (i.e., same concentration of catalysts and at the concentration of their corresponding CAC), maximum reaction rate V_{max} of *F*-chain was far higher than that of its *H*-chain counterpart. The catalysis experiments under the condition of a fixed substrate concentration while increasing *F*-chain or *H*-chain concentration in the presence of equimolar metal ions revealed that not only apparent first order rate constants at assembly state are always higher than those at non-assembly state, but also for assembly state, apparent first order rate constants of *F*-chain are far higher than those of *H*-chain. Yet it was the opposite for Michaelis-Menten constant K_M, supporting the strong affinity of *F*-chain assemblies with HPNP and their high catalytic activity. Coarse-grained molecular dynamics (CGMD) simulations with the MARTINI 3.0 force field were also carried out to gain insight into this powerful catalytic ability of *F*-chain assemblies driven by coordination to Zn^{2+} ions. In addition to Zn^{2+} ions, these *F*-chains were also capable of coordinating Cu^{2+} ions to form aggregates, affording a lower CAC (1 order of magnitude, compared to that of its *H*-chain counterpart). This Cu^{2+} coordination-driven assembly could catalyze the oxidation reaction of a traditional substrate *o*-phenylenediamine (OPD), like that of an oxidase. Furthermore, catalysis modulation and reusability experiments illustrated the robustness of the supramolecular assembled *F*-chain catalyst.

Results and Discussion

TACN derivatives and substrate synthesis

Three TACN derivatives bearing a linear F_nH_m diblock, namely C_6F_{13}-C_2H_4-TACN, $C_{10}F_{21}$-C_2H_4-TACN, and C_8F_{17}-C_3H_6-TACN (Scheme 2), in which the carbon atom number of the terminated perfluoroalkyl chain varies from 6 to 10 and the short-linked *H*-chain is 2 or 3, were designed and synthesized. The perhydroalkyl derivative $C_{11}H_{23}$-TACN was also synthesized as a reference in this study. All synthetic routes and procedures are described in Schemes S1-S4. The substrate HPNP was synthesized via a one-step ring-opening reaction (Scheme S5).[6]

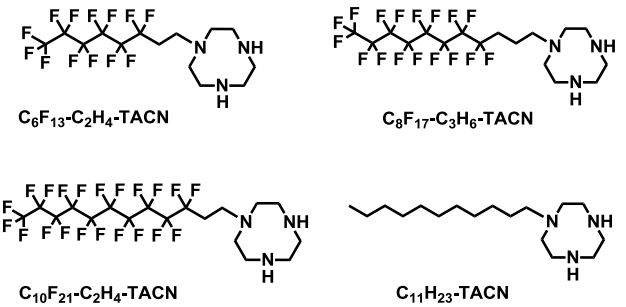

Scheme 2. Molecular structures of polyfluorinated C_nF_{2n+1}-C_mH_{2m}-TACN and the control compound perhydroalkyl $C_{11}H_{23}$-TACN considered and synthesized in this work.

Zn^{2+} coordination-driven self-assembly of TACN derivatives

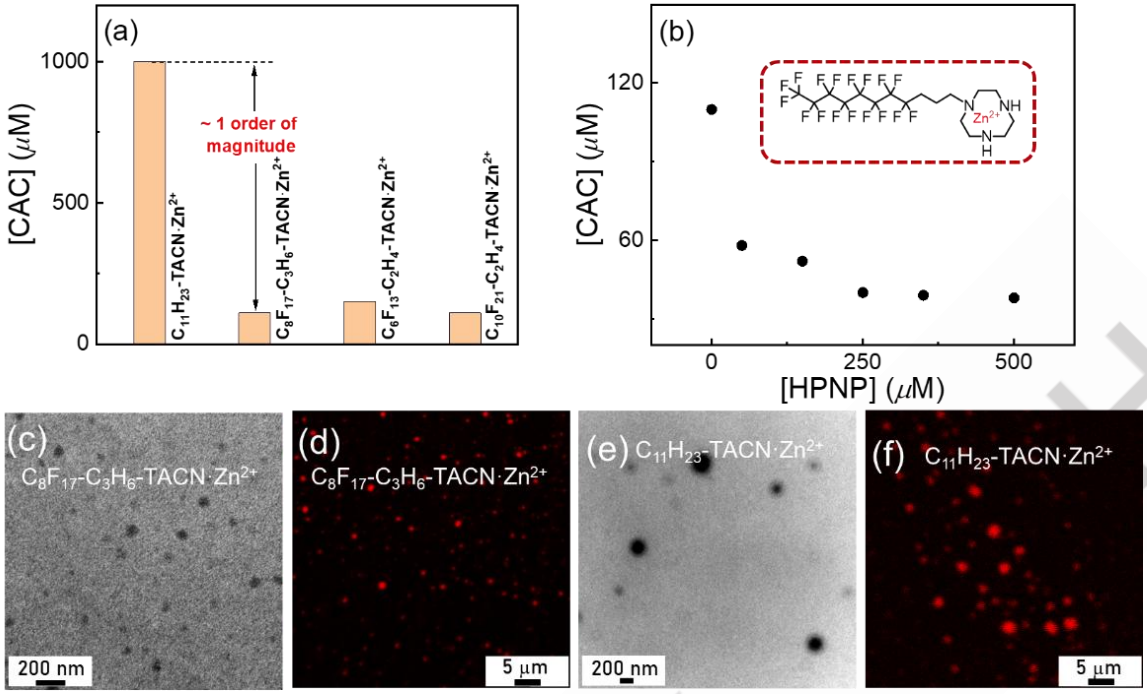

Figure 1. (a) Comparison of CAC values of polyfluorinated C_nF_{2n+1}-C_mH_{2m}-TACN·Zn^{2+} and perhydroalkyl $C_{11}H_{23}$- TACN·Zn^{2+}. (b) HPNP concentration-dependent CAC values of C_8F_{17}-C_3H_6-TACN·Zn^{2+}. TEM (c and e) and CLMS (d and f) images of C_8F_{17}-C_3H_6-TACN·Zn^{2+} (c and d) and $C_{11}H_{23}$-TACN·Zn^{2+} (e and f) assemblies.

Assembly and catalysis were then studied, first in the presence of Zn^{2+} ions. Assuming the molar ratio of the complexation of TACN moiety to Zn^{2+} ions is 1:1,[16] equimolar amount of Zn^{2+} ions were added to a C_nF_{2n+1}-C_mH_{2m}-TACN aqueous solution to create surfactant-like molecules bearing one hydrophilic head and a long hydrophobic alkyl chain.

First, the CAC of C_nF_{2n+1}-C_mH_{2m}-TACN·Zn^{2+} surfactants was determined by using Nile Red (NR), which does not emit fluorescence in an aqueous or polar environment and does emit fluorescence in a lipophilic environment. Despite the incompatibility of the *F*-chain with NR due to its fluorophiphilicity, the short *H*-chain act as a spacer between *F*-chain and the TACN moiety, and is expected to allow the formation of a hydrophobic microenvironment during self-assembly for the encapsulation of NR. Compared to the CAC value (450 μM) of the shortest *F*-chain C_6F_{13}-C_2H_4-TACN·Zn^{2+}, both CAC values of C_8F_{17}-C_3H_6-TACN·Zn^{2+} and $C_{10}F_{21}$-C_2H_4-TACN·Zn^{2+} significantly decreased to ~110 μM (Figures S1a, b, and c and Table S1). This decrease in CAC indicated that the long *F*-chain surfactant has a stronger tendency to aggregate in aqueous solution than those from short *F*-chains. We should note that the $C_{10}F_{21}$-C_2H_4-TACN and C_8F_{17}-C_3H_6-TACN surfactants have almost the same CAC values, although the *F*-chain carbon atom number in C_8F_{17}-C_3H_6-TACN is smaller than that in $C_{10}F_{21}$-C_2H_4-TACN. To further verify the strong tendency of *F*-chains to aggregate in aqueous solution, the CAC of perhydroalkyl chain $C_{11}H_{23}$-TACN was also measured and compared with that of the C_8F_{17}-C_3H_6-TACN polyfluorinated counterpart, with same total carbon atom number of alkyl chains (Figures S1b and d). We were pleased to observe that the CAC of polyfluorinated C_8F_{17}-C_3H_6-TACN·Zn^{2+} is lower by ~1 order of magnitude than that of its perhydroalkyl chain counterpart, ~1000 μM (Figure 1a). This substantial decrease provides important evidence for the supra-hydrophobicity of *F*-chains. Regretfully, longer *F*-chains are not yet commercially available at present to synthesize longer C_nF_{2n+1}-C_mH_{2m}-TACN chains, with similar synthesis procedure, to further decrease the CAC to μM magnitude. We can envision that, even in the absence of Zn^{2+} ions, C_nF_{2n+1}-C_mH_{2m}-TACN could also show a tendency to aggregate in aqueous solution when its concentration is increased, given that the terminated head of TACN possesses a certain degree of hydrophilicity. Experimental measurements of C_nF_{2n+1}-C_mH_{2m}-TACN CAC in the absence of Zn^{2+} ions could support this assumption (Figure S2 and Table S1), although their CAC values were higher than those of the corresponding counterparts in the presence of equimolar amount of Zn^{2+} ions, in all cases, confirming the importance of Zn^{2+} ions coordination to lower CAC. To confirm the assumed binding ratio of C_nF_{2n+1}-C_mH_{2m}-TACN (or $C_{11}H_{23}$-TACN) to Zn^{2+} ions, UV-vis absorption spectral titration experiments were conducted in the presence of 80 μM HPNP as the substrate when C_nF_{2n+1}-C_mH_{2m}-TACN (or $C_{11}H_{23}$-TACN) concentrations were set above CAC values of corresponding surfactants formed via the complexation of equimolar amount of Zn^{2+} ions. All spectral results supported the assumed 1:1 binding ratio of C_nF_{2n+1}-C_mH_{2m}-TACN (or $C_{11}H_{23}$-TACN) to Zn^{2+} ions (Figure S3). Considering the anionic nature of the substrate HPNP, which is able to interact with one or multiple positive TACN·Zn^{2+} head(s) via electrostatic attractive interaction,[17] we further measured the CAC values of C_nF_{2n+1}-C_mH_{2m}-TACN·Zn^{2+} (or $C_{11}H_{23}$-TACN·Zn^{2+}) surfactants in the presence of different concentrations of HPNP. We found that with increasing HPNP concentration, the CAC values rapidly decreased (Figure 1b and Figure S4). This observation supported that HPNP can serve as a linker by binding one or multiple positive TACN·Zn^{2+} head(s)

through attractive electrostatic interactions, resulting in a significant improvement on the assembly behaviors.[17] Transmission electron microscopy (TEM) revealed the formation of micelle-like assemblies of C_nF_{2n+1}-C_mH_{2m}-TACN·Zn^{2+}, although these assemblies appear difficult to distinguish in terms of morphology (Figures 1c, e, and Figure S5). Confocal laser microscopy (CLMS) further supported the formation of micelle-like assembly morphologies, using NR as the fluorescent probe (Figures 1d, f, and Figure S6). We should note that the observed assembies in both TEM and CLMS images maybe the aggregates of initially formed micelles or multilayer-micelles, considering that the observed sizes of assemblies are somewhat big.

Catalytic efficiency

On the basis of the aforementioned findings, it was expected that a strong catalytic effect would be proven. Solid evidence for catalysis was obtained from HRMS experiments. The signal peak of m/e at 138.0196, could be ascribed to that of *p*-nitrophenolate anion, due to its theoretical m/e value at 138.0197 (Figure S7). When both equimolar amount of C_8F_{17}-C_3H_6-TACN and Zn^{2+} ions (120 μM, higher than its CAC) were mixed in 10 mM HEPES buffer solution of pH 7.4, significant absorbance at 400 nm increased with extending scanning-time (Figure 2a). This absorption could be ascribed to that of hydrolyzed *p*-nitrophenolate anion due to its strong charge transfer (CT).[18] However, for its perhydroalkyl chain counterpart $C_{11}H_{23}$-TACN·Zn^{2+} under the same concentration, far from reaching the concentration for its assembly, almost no significant UV-vis absorption spectral change was observed (see inset in Figure 2a). This observation clearly supported that assembly is the prerequisite for the catalysis. Other control experiments revealed that significant catalysis for the hydrolysis reaction of HPNP was absent under same experimental conditions (Figure 2b). To the compare the catalytic activity between C_8F_{17}-C_3H_6-TACN·Zn^{2+} and $C_{11}H_{23}$-TACN·Zn^{2+} (to keep same number of total carbon atoms in the alkyl chains), two groups of experiments were conducted to fit Michaelis-Menten equation curves: (i) identical surfactant concentrations, namely, 1000 μM C_8F_{17}-C_3H_6-TACN·Zn^{2+} (1 of Figure 2c) and 1000 μM $C_{11}H_{23}$-TACN·Zn^{2+} (3 of Figure 2c), and (ii) both C_8F_{17}-C_3H_6-TACN·Zn^{2+} and $C_{11}H_{23}$-TACN·Zn^{2+} concentrations were set to their corresponding CAC values without HPNP (110 μM and 1000 μM, respectively). We were pleased to observe, not only under respective CAC concentration (110 μM of C_8F_{17}-C_3H_6-TACN·Zn^{2+} and 1000 μM of $C_{11}H_{23}$-TACN·Zn^{2+}), V_{max} of C_8F_{17}-C_3H_6-TACN·Zn^{2+} was higher than that of $C_{11}H_{23}$-TACN·Zn^{2+} (>1 order of magnitude), but also under identical surfactant concentration (both at their assembly state), V_{max} of C_8F_{17}-C_3H_6-TACN·Zn^{2+} was also much higher than that of $C_{11}H_{23}$-TACN·Zn^{2+} (159 ± 6.00 ×10^{-8} M·s^{-1} *vs.* 5.13 ± 0.06 ×10^{-8} M·s^{-1}), up to more thant 1 order of magnitude (Figures 2c, d), and K_M of C_8F_{17}-C_3H_6-TACN·Zn^{2+} was lower than that of $C_{11}H_{23}$-TACN·Zn^{2+} (1.66 mM *vs.* 3.29 mM). The Michaelis-Menten fitting curves of C_nF_{2n+1}-C_mH_{2m}-TACN·Zn^{2+} to HPNP are shown in Figure S8, and the corresponding fitting data are shown in Table S2. The turnover of C_8F_{17}-C_3H_6-TACN·Zn^{2+} assemblies is moderate (~4 of 5 h; Figure S9). Considering the addition of HPNP is likely to affect the equilibrium between C_8F_{17}-C_3H_6-TACN·Zn^{2+} assemblies ("real catalytic sites") and non-assembled states,[17]

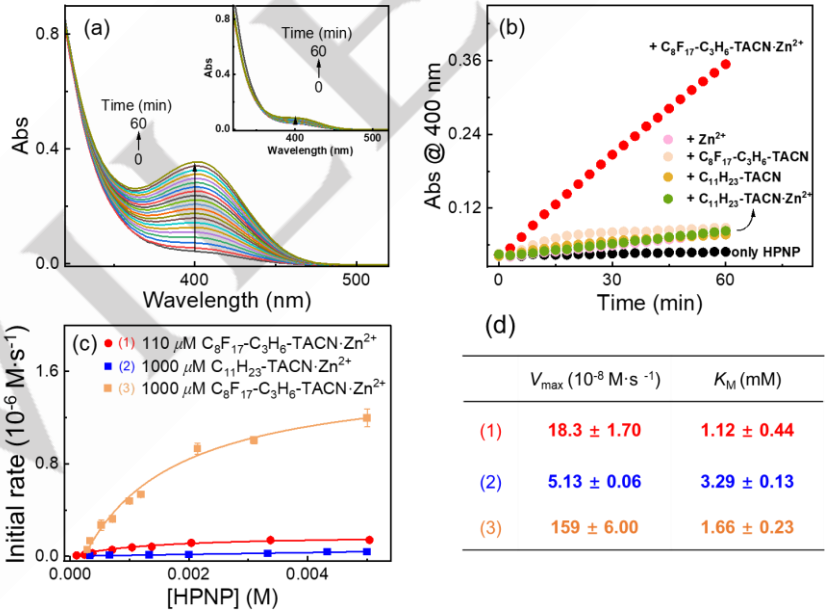

(d)

	V_{max} (10^{-8} M·s^{-1})	K_M (mM)
(1)	18.3 ± 1.70	1.12 ± 0.44
(2)	5.13 ± 0.06	3.29 ± 0.13
(3)	159 ± 6.00	1.66 ± 0.23

Figure 2. (a) Incubation time-dependent UV-vis absorption spectral change of 200 μM HPNP in 10 mM HEPES buffer solution of pH 7.4 in the presence of 120 μM C_8F_{17}-C_3H_6-TACN·Zn^{2+}, or of 120 μM $C_{11}H_{23}$-TACN·Zn^{2+} (inset in a), and (b) incubation time –dependent Abs@400 nm change curves of HPNP solution in the absence and presence of other additives (other control cases, experiment condition: 10 mM HEPES buffer solution at pH 7.4, [C_8F_{17}-C_3H_6-TACN] = [$C_{11}H_{23}$-TACN] = [Zn^{2+}] = 120 μM, [HPNP] = 200 μM). (c) Initial rate as a function of HPNP concentration in the presence of C_8F_{17}-C_3H_6-TACN·Zn^{2+} (1, red line) and $C_{11}H_{23}$-TACN·Zn^{2+} (2, blue line), at respective CAC and 1000 μM C_8F_{17}-C_3H_6-TACN·Zn^{2+} (3, yellow line), fitted by the Michaelis-Menten equation. (d) Fitted V_{max} and K_M in (c) curves. Experimental conditions (c and d): 10 mM HEPES buffer solution of pH 7.4; temperature was set as 37 °C. All error bars in this work were obtained through measuring three parallel experiments.

indeed it is difficult for us to accurately know the real concentration of assembled catalysts to accurately afford the absolute catalytic efficiency (k_{cat} = V_{max}/[catalyst]) although k_{cat} values were also roughly assessed (Table S2). Therefore, it is reasonable for that V_{max}, measured under the aforementioned experimental conditions, was used to compare the catalytic activity in this work. Importantly, to afford more convincing evidence, we did the catalysis experiments under the condition: a fixed substrate concentration while increasing *F*-chain (C_8F_{17}-C_3H_6-TACN) or *H*-chain ($C_{11}H_{23}$-TACN) concentration in the presence of equimolar Zn^{2+} ions (Figure 3a). We can obtain several intriguing points from Figure 3: (i) Sigmoidal curve profiles seem to appear, in particular C_8F_{17}-C_3H_6-TACN·Zn^{2+} case. Regretfully, we could not further increase C_8F_{17}-C_3H_6-TACN·Zn^{2+} concentration when its concentration exceeded 1800 μM due to the occurrence of apparent precipitates which can interfere the spectral measurement. (ii) The apparent first order rate constants at assembly state are always higher than those at non-assembly state. (iii) For assembly state, apparent first order rate constants of *F*-chain are far higher than those of *H*-chain. For example, the maximum difference can be observed to *ca*. 27 times in Zn^{2+}-based catalysts. Thereofe, taken together, we can conclude that not only the catalytic activity but also the affinity of *F*-chain assemblies towards the substrate are higher than those of *H*-chain assemblies.

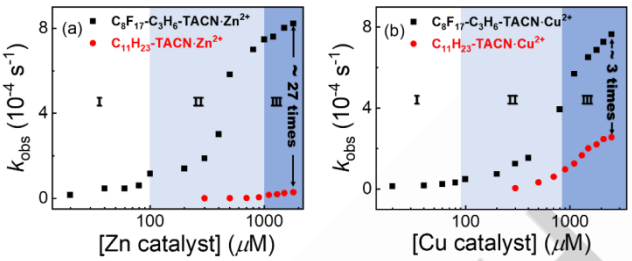

Figure 3. The comparison between C_8F_{17}-C_3H_6-TACN (black squares) and $C_{11}H_{23}$-TACN (red circles) in the presence of equimolar Zn^{2+} (a) or Cu^{2+} (b) in the relationship between k_{obs} and catalyst concentration (fixed HPNP concentration as 200 μM). For *F*-chain in the presence of equimolar metal ions, "I" region represents the non-assembly state; "II" and "III" regions represent the assembly state. For *H*-chain in the presence of equimolar metal ions, "II" region represents the non-assembly state; "III" region represents the assembly state.

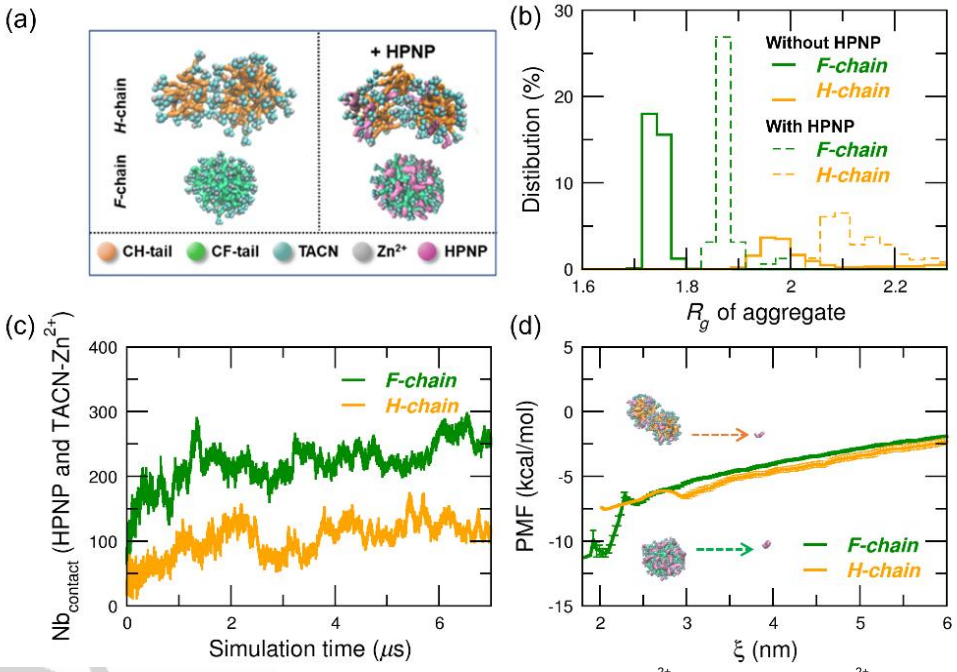

Figure 4. Comparison of the morphology (a) and radius of gyration (b) of the C_8F_{17}-C_3H_6-TACN·Zn^{2+} and $C_{11}H_{23}$-TACN·Zn^{2+} assemblies in the absence (solid lines) or in the presence (dash lines) of HPNP during their aggregation processes simulated by using CGMD. (c) The change of contact number of HPNP to aggregates with increasing simulation time, in both cases of C_8F_{17}-C_3H_6-TACN·Zn^{2+} (green line) and $C_{11}H_{23}$-TACN·Zn^{2+} (yellow line). (d) Potentials of the mean force (PMF) calculated along the z-axis coordinates for pulling HPNP away from the COM of the rest of the $C_{11}H_{23}$-TACN·Zn^{2+} (orange) and C $_8F_{17}$-C_3H_6-TACN·Zn^{2+} (green) aggregates. Relatively few bins (200) have been used to generate this figure.

Coarse-grained molecular dynamics simulations

To gain deeper insight into the difference in catalytic properties between polyfluorinated C_nF_{2n+1}-C_mH_{2m}-TACN·Zn^{2+} and perhydroalkyl chain $C_{11}H_{23}$-TACN·Zn^{2+} self-assemblies, CGMD simulations were performed in explicit water with 150 mM NaCl. To reasonably shorten the simulation time, we considered 5 mM of C_8F_{17}-C_3H_6-TACN·Zn^{2+} and $C_{11}H_{23}$-TACN·Zn^{2+} surfactants, corresponding to a number of 72 chains in each system.

Starting from separated chains, the assembled state of each system was monitored by computing both the number of aggregates and the size of the largest one as a function of time (Figure S10). In both C_8F_{17}-C_3H_6-TACN·Zn^{2+} and $C_{11}H_{23}$-TACN·Zn^{2+} systems, we could observe the formation of a single nanoparticle after about 6 μs. However, in the absence or presence of HPNP, we note that the perhydroalkyl $C_{11}H_{23}$-TACN·Zn^{2+} aggregates are less stable than the *F*-chain C_8F_{17}-C_3H_6-TACN·Zn^{2+} counterpart (Figure S10a and S10c vs. Figure

S10b and S10d). This is confirmed by monitoring the Gibbs free energy the *H*-chain system which always appears higher than that of the *F*-chain counterpart, with or without HPNP (Figures S10e and S10f). This difference in thermodynamics confirmed that *F*-chains have a stronger tendency to aggregate in aqueous micelle-like structures rather than vesicle-like structures (Figure 4a), confirming the observations by TEM and CLMS. It could be noted that the morphology of the F-chain aggregates appears more spherical than that of the perhydroalkyl ones. Analysis of the radius of gyration also revealed that *F*-chain assemblies were more compact than *H*-chains (Figure 4b). CGMD simulations further indicated that the addition of HPNP did not significantly change the morphology and size of both C_8F_{17}-C_3H_6-TACN·Zn^{2+} and $C_{11}H_{23}$-TACN·Zn^{2+} aggregates which retain their micelle-like structures (Figure 4a).

Upon the addition of HPNP to each system, the number of contacts between HPNP and TACN heads (when the distance between the substrate and the catalytic head is smaller than 0.5 nm) rapidly increases and seems to reach a plateau after 2 μs in both C_8F_{17}-C_3H_6-TACN·Zn^{2+} and $C_{11}H_{23}$-TACN·Zn^{2+} assemblies (Figure 4c). However, the *F*-chain micelle can make twice as many contacts with HPNP substrate than the *H*-chain micelle (Figure 4c and Figure S11). This result showed a lower affinity of HPNP towards $C_{11}H_{23}$-TACN·Zn^{2+} than towards C_8F_{17}-C_3H_6-TACN·Zn^{2+} assemblies, as confirmed by our binding free energy calculations using Umbrella Sampling simulations. Indeed, the computed free energy profiles (FEP) of a HPNP substrate as a function of its distance to the center of each micelle, indicating that with the HPNP binding free energy to C_8F_{17}-C_3H_6-TACN-Zn^{2+} micelle-like aggregate is about -11.3 ± 0.6 kcal/mol, whereas it is only about -7.5 ± 0.1 kcal/mol to $C_{11}H_{23}$-TACN-Zn^{2+} assembly (Figure 4d, and Figure S12). Altogether, the two aforementioned differences (micelle stability and HPNP contact number) could well explain the experimentally observed difference in substrate binding affinity and catalytic activity between *F*-chain and *H*-chain self-assemblies (Figures 2c, 2d).

Finely modulated, extended and robust biomimetic catalysis

This favorable assembly of *F*-chain in aqueous solution can be further featured to demonstrate its robustness through the modulation of its catalytic activity. Ethylene diamine tetra-acetic acid (EDTA) was chosen to try to recover Zn^{2+} ions from TACN·Zn^{2+} heads considering it is a well-known metal ligand in coordination chemistry. From Figure 5, we observed that when equimolar amount of EDTA were added to a 110 μM C_8F_{17}-C_3H_6-TACN·Zn^{2+} buffer solution in the presence of 600 μM HPNP, in the first round addition, catalysis was completely turned off, as the time-dependent Abs@400 nm curve plateaued (Figure 5a). The extremely high binding stability constant[19] of EDTA to Zn^{2+} ions (log*k* = 16.4) meant that all Zn^{2+} ions were removed from the TACN·Zn^{2+} heads[20] in this catalytically silent curve profile (starting from first addition of EDTA and ending from second addition of Zn^{2+} ions), due to the competition reaction between TACN and EDTA to complex Zn^{2+} ions. However, when equimolar amount of Zn^{2+} ions were added again, the catalysis was turned on. Such reversibility cycle could be repeated at solution than the perhydroalkyl ones, supporting their lower CAC values. The greater stability of polyfluorinated TACN derivatives should probably induce a better catalysis efficiency.

The fully equilibrated aggregate coarse-grained models show that both *F*-chain and *H*-chain surfactants tend to form least 3 times (Figures 5a, c). The catalysis process could be finely manipulated using one-third of equimolar amount of EDTA (33.3% of 110 μM) in each addition (Figure 5b). We observed that the increase in absorbance became gradually slower with each addition, and by the third addition, catalysis was almost extinguished. This also confirms the well-known 1:1 molar ratio of EDTA complexation to metal ions. Such fine manipulation of catalysis could be still achieved even if third round addition was conducted. No significant fluorescent assemblies could be observed in CLMS images after the introduction of equimolar EDTA into 110 μM C_8F_{17}-C_3H_6-TACN·Zn^{2+} assemblies (Figure 5d), supported the disassembly. Furthermore, to verify the importance of carboxylic groups of EDTA in this excellent ability to modulate the catalysis of C_8F_{17}-C_3H_6-TACN·Zn^{2+} assemblies, nitrilotriacetic acid (3-NA), iminodiacetic acid (2-IA) and *β*-alanine (1-BA), were used to substitute EDTA in order to tune the catalysis, considering they contain three, two, and one –COOH group(s), respectively (Figure 5e). The ability of manipulating the catalysis decreased with decreasing the number of carboxylic groups from the binding ligands (Figure S13). This likely resulted from the difference in binding ability of these ligands to Zn^{2+} ions. Therefore, the excellent modulation performance can demonstrate the robustness of C_8F_{17}-C_3H_6-TACN·Zn^{2+} assemblies, compared with that of perhydroalkyl $C_{11}H_{23}$-TACN·Zn^{2+} that failed in such modulation (Figure S14).

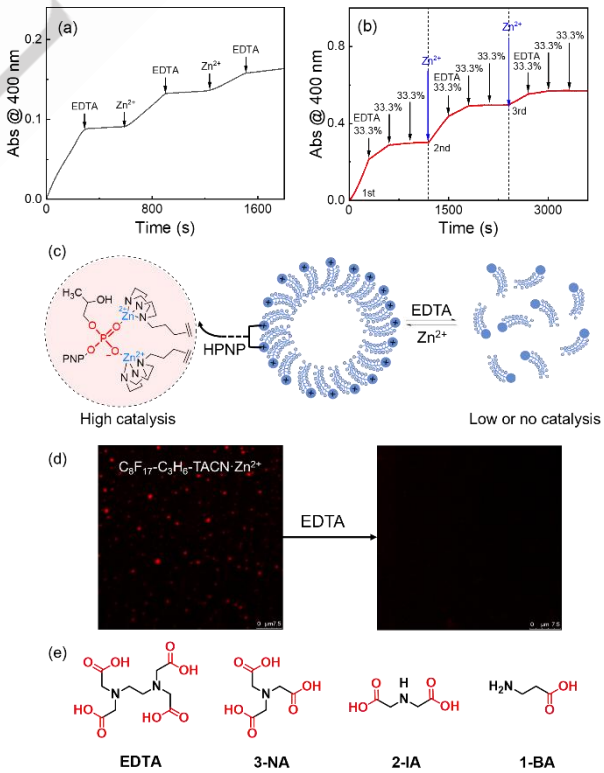

Figure 5. The change curve of Abs@400 nm of 110 μM C_8F_{17}-C_3H_6-TACN·Zn^{2+} assemblies in the presence of 600 μM HPNP with extending reaction time, successively added equimolar amount of EDTA and Zn^{2+} (a)

and added 3 parts of one-third equimolar amount of EDTA and 3 parts of one-third equimolar amount of Zn^{2+}, in turn (b). The schematic diagram of Zn^{2+}-induced assembly and disassembly induced by EDTA, and the catalysis to substrate HPNP, of the assembled state (c). The comparison of CLMS images of 110 μM C_8F_{17}-C_3H_6-TACN·Zn^{2+} assemblies between before and after added equimolar EDTA in the presence of NR (d). The molecular structures of EDTA, 3-NA, 2-IA and 1-BA (e).

Inspired by the aforementioned Zn^{2+} coordination-driven catalysis, we were interested to see how assembly and catalytic activity proceeded when Zn^{2+} ions were replaced by other metal ions such as redox-active Cu^{2+} ions. First, we attempted to use NR fluorescence to measure the CAC value based on an assumed 1:1 of molar ratio of C_8F_{17}-C_3H_6-TACN to Cu^{2+}. However, Cu^{2+} ions were found to seriously quench the fluorescence of NR dye. Therefore, another traditional fluorescent dye, 1,6-diphenyl-1,3,5-hexatriene (DPH), was used instead. As shown in Figure 6a, the CAC of C_8F_{17}-C_3H_6-TACN·Cu^{2+} is ~ 90 μM, which is 1 order of magnitude lower than that of the perhydroalkyl counterpart, ~ 900 μM (Figure S15). Furthermore, we used the initial rate method to measure the CAC values with HPNP as the substrate (Figure S16). These CAC values were found to match well with those measured by fluorescence. TEM experiments also revealed the micelle-like morphology of C_8F_{17}-C_3H_6-TACN·Cu^{2+} assemblies (Figure 6e). HPNP was used as the substrate to probe the catalysis of C_8F_{17}-C_3H_6-TACN·Cu^{2+} assemblies. First, UV-vis absorption spectral titration experiments supported the 1:1 of molar ratio of C_8F_{17}-C_3H_6-TACN to Cu^{2+} ions (Figure 6b). Interestingly, a very impressive sigmoidal curve profile was observed, indicated a good cooperativity, [21] originated from the two neighboring Cu^{2+} ions to catch one HPNP molecule to form an effective catalytic pocket. Similar to C_8F_{17}-C_3H_6-TACN·Zn^{2+} case, we further conducted the catalysis experiments under condition of fixed HPNP concentration as 200 μM while increasing C_8F_{17}-C_3H_6-TACN·Cu^{2+} concentration (Figure 3b). The catalytic activity of C_8F_{17}-C_3H_6-TACN·Cu^{2+} assemblies towards HPNP are significantly higher than those of the corresponding *H*-chain case, too. For exapmle, the maximum difference can reach ~ 3 times (Figure 3b).

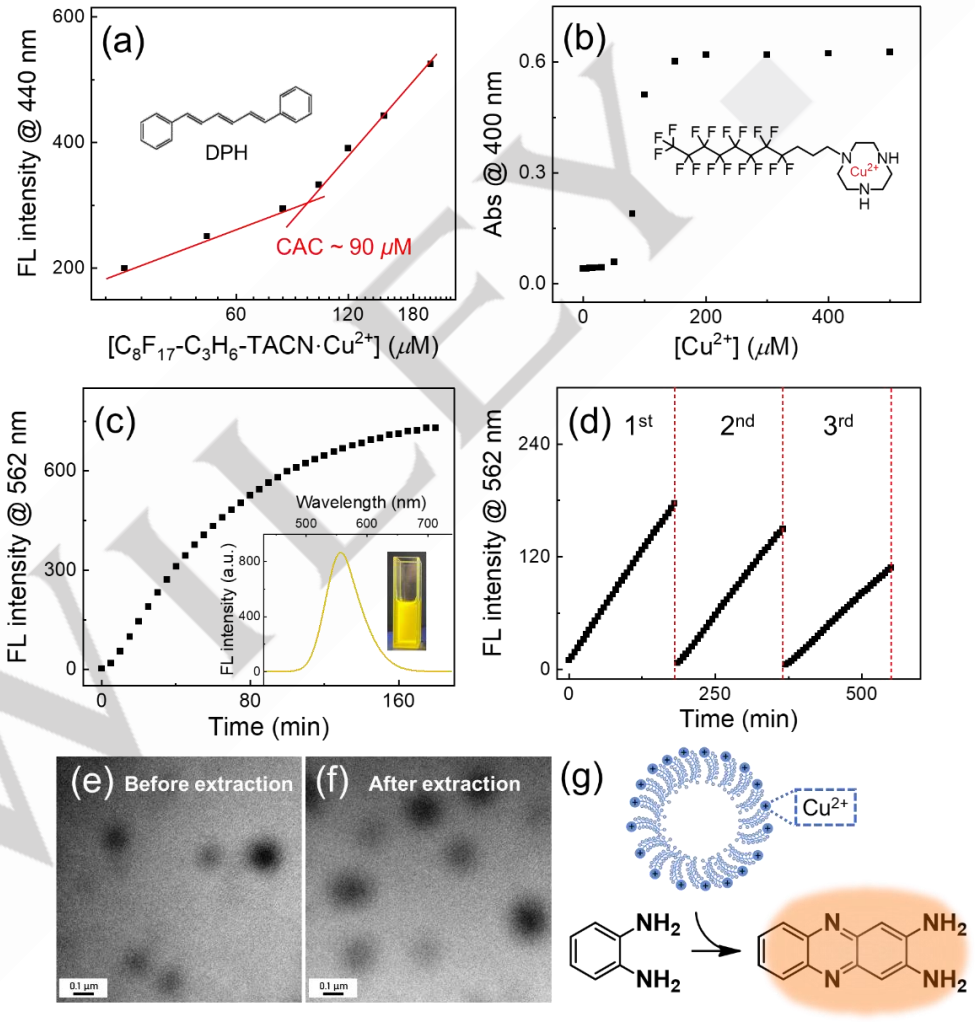

Figure 6. (a) The CAC value of C_8F_{17}-C_3H_6-TACN·Cu^{2+} was determined by using DPH fluorescent probe. (b) The coordination ratio titration curves of C_8F_{17}-C_3H_6-TACN to Cu^{2+} ions in the presence of HPNP as the substrate ([C_8F_{17}-C_3H_6-TACN] = 200 μM). (c) The relationship curve between fluorescence intensity@562 nm and reaction time, in 200 μM OPD solution catalyzed by C_8F_{17}-C_3H_6-TACN·Cu^{2+} assemblies (d). The fluorescence intensity as a function of the reaction time for OPD oxidation reaction catalyzed by C_8F_{17}-C_3H_6-TACN·Cu^{2+} assemblies, for three repeated rounds. (e) and (f) are TEM images of C_8F_{17}-C_3H_6-TACN·Cu^{2+} assemblies in aqueous solution and separated to fluorine phase solution, respectively. (g) The schematic diagram of OPD oxidation reaction catalyzed by C_8F_{17}-C_3H_6-TACN·Cu^{2+} assemblies.

Considering the possible intrinsic redox-active nature of the aforementioned TACN·Cu^{2+} head, we attempted to broaden the scope of substrates. OPD is a traditional substrate for many oxidases.[22] Therefore, we used OPD to evaluate C_8F_{17}-C_3H_6-TACN·Cu^{2+} assemblies as an oxidase mimic. It was found that in HEPES buffer solution (10 mM, pH of 7.4), originally non-fluorescent C_8F_{17}-C_3H_6-TACN·Cu^{2+} solution containing 200 μM OPD gradually became yellow emissive with increasing the reaction time, with a maximum emission wavelength at 562 nm (see inset in Figure 6c). This maximum fluorescence wavelength is identical to that of reported cases,[23] supporting the formation of 2, 3-diaminophenazine, an oxidized product of OPD (Figure 6g). Therefore, this observation indicates that C_8F_{17}-C_3H_6-TACN·Cu^{2+} assemblies can function as a good oxidase mimic (Table S3), which demonstrates the diversity of its catalyst role. We further envisaged using a "fluorous" phase to extract C_8F_{17}-C_3H_6-TACN·Cu^{2+} assemblies from an aqueous solution phase due to the fluorophilicity of C_8F_{17}-C_3H_6-TACN, to investigate its ability of repeatable usage. From the repeated cycle experiment (Figure 6d, and procedure refers to experimental section), we conclude that such *F*-chain-based catalyst can demonstrate a favorable separability and repeatability, for at least 3 times. Even if at third round, good catalytic ability to OPD could be still shown. However, we could not successfully do such repeated experiments with the corresponding perhydroalkyl chains. Importantly, TEM was used to confirm that the micelle-like morphology of the assembled C_8F_{17}-C_3H_6-TACN·Cu^{2+} catalyst could be retained after the phase transfer step (Figure 6f). Such unchanged assembly morphology is important for maintaining catalytic capacity, which also illustrates its robustness.

Conclusion

In conclusion, on the basis of supra-assembly ability of highly fluorinated alkyl chain-based compounds, a series of TACN derivatives bearing a highly fluorinated alkyl chain with varying lengths, C_nF_{2n+1}-C_mH_{2m}-TACN, were designed and synthesized. Zn^{2+} coordination-driven assembly of *F*-chain afforded a lower CAC compared to its *H*-chain counterpart in aqueous solution. In addition to Zn^{2+} ions, coordination of Cu^{2+} ions can also drive *F*-chain based TACN derivative to show a lower CAC value and to afford diverse catalytic properties such as the oxidation reaction of OPD, acting as an oxidase mimic. Such *F*-chain assembly exhibited several important features: (i) more compact and stable assembling structure, (ii) higher binding ability to substrate and higher catalytic activity, (iii) favorable separability and repeatability, demonstrating the robustness of *F*-chain assemblies. Furthermore, the catalytic activity of this robust *F*-chain catalyst could be finely modulated through the successive addition of EDTA and Zn^{2+}. Although longer fluorinated alkyl chains are not commercially available, the aforementioned advantages of *F*-chain assemblies can open a new avenue for creating novel and robust catalytic supramolecular assemblies and artificial enzymatic mimics, which is also beneficial from the perspective of atomic economy.

Experimental and Computational Section

Synthesis and characterization:
TACN derivatives containing a linear F_nH_m diblock, in which the carbon atomic number of the terminated *F*-chain is from 6 to 10 and of the short-yoked *H*-chain is 2 or 3, were synthesized, named C_6F_{13}-C_2H_4-TACN, C_8F_{17}-C_3H_6-TACN, $C_{10}F_{21}$-C_2H_4-TACN, and $C_{11}H_{23}$-TACN, respectively (Schemes S1-S4). For detailed synthetic procedures, please refer to "1. Synthesis and characterization of TACN derivatives and substrate HPNP" section in the supporting information. The substrate HPNP was synthesized via a one-step ring-opening reaction (Scheme S5).

UV–vis absorption spectral titration experiments:
UV–vis absorption spectral titration experiments of C_nF_{2n+1}-C_mH_{2m}-TACN to Zn^{2+}. First, 600 μM C_6F_{13}-C_2H_4-TACN, 200 μM C_8F_{17}-C_3H_6-TACN, 200 μM $C_{10}F_{21}$-C_2H_4-TACN, or 1200 μM $C_{11}H_{23}$-TACN stock solution, respectively, was added to 10 mM HEPES buffer solution (pH 7.4) containing 100 μM HPNP to obtain a total volume of 3 mL, and Zn^{2+} ions stock solution were then added dropwise (the final concentration was varied from 0 to 1200 μM) to monitor the UV-vis absorption spectral change of the resulting solution using a UV–vis absorption spectrometer (UV-2600, Shimadzu, Japan) at 37 °C for 30 min.

UV–vis absorption spectral titration experiments of C_8F_{17}-C_3H_6-TACN to Cu^{2+}. First, 200 μM C_8F_{17}-C_3H_6-TACN solution was added to 10 mM HEPES buffer solution (pH 7.4) to obtain a total solution volume of 3 mL, and Cu^{2+} were then added dropwise (the final concentration was varied from 0 to 500 μM) to monitor the UV-vis absorption spectral change of the resulting solution using a UV–vis absorption spectrometer (UV-2600, Shimadzu, Japan) at 37 °C for 30 min.

Michaelis-Menten equation kinetics:
The hydrolysis reactions of HPNP catalyzed by C_nF_{2n+1}-C_mH_{2m}-TACN·Zn^{2+} assemblies (n = 6, 8, and 10; m = 2 and 3) were probed by measuring the change of the reaction time dependent-absorbance at 400 nm wavelength, respectively. A certain volume of C_nF_{2n+1}-C_mH_{2m}-TACN·Zn^{2+} stock solution and a series of volumes of 50 mM HPNP stock solution (from 0 to 400 μL) were mixed in 5 mL glass test tubes, respectively. The total solution volume of each test tube was kept as 3 mL by adding a certain volumes of 10 mM HEPES buffer solution of pH 7.4, leading to the final concentration of C_nF_{2n+1}-C_mH_{2m}-TACN·Zn^{2+} was as the corresponding CAC concentrations and the final concentration of substrate was from 0 to 10 mM.

For $C_{11}H_{23}$-TACN·Zn^{2+}, its concentration was set as 110 μM, equal to the CAC of C_8F_{17}-C_3H_6-TACN·Zn^{2+}, to compare V_{max} value at the same concentration. 33 μL 10 mM C_8F_{17}-C_3H_6-TACN·Zn^{2+} stock solution and a series of volumes of 50 mM substrate stock solution (from 0 to 400 μL) were mixed in 5 mL test tubes, respectively. The total solution volume was kept as 3 mL by adding a certain volumes of 10 mM HEPES buffer solution of pH 7.4, leading to the final concentration of substrate was from 0 to 5 mM.

The initial rate was calculated from the reaction time dependent-absorbance of *p*-nitrophenol anion at 400 nm evolving curves. The molar absorption coefficient (ε) of *p*-nitrophenol anion was measured to 8918.98 $L \cdot mol^{-1} \cdot cm^{-1}$. Absorbance at 400 nm of the reaction solution was recorded by

a UV-2600 spectrometer (Shimadzu, Japan) in which the scanning time was extended to 5 min at 37 °C.

ESI-MS experiments for probing the hydrolysis reactions:
C_8F_{17}-C_3H_6-TACN·Zn^{2+} assembly concentration was set as 110 μM, the substrate concentration was set as 800 μM, and the temperature was kept at 37 °C for 30 min. The reaction solution was then injected into an ESI-MS system for obtaining desirable ESI-MS spectra.

CAC was determined using fluorescence probes (NR and DPH method) and initial rate method:
NR fluorescence method: 10 μL 1.0 mM NR stock solution and 1 mL 10 mM HEPES buffer solution of pH 7.4 were added into a 3 mL test tube to afford 10 μM NR solution. Several such NR solutions were prepared. After that, different amounts of C_nF_{2n+1}-C_mH_{2m}-TACN·Zn^{2+} were added into each test tube, respectively, and these test tubes were kept for 15 min at 37 ^oC to record their fluorescence spectra. The excitation wavelength was used as 564 nm. The experiments are carried out on a F-7000 fluorescence spectrometer (Hitachi, Japan).

DPH fluorescence method: The procedure of DPH fluorescence method was similar to that of NR fluorescence method. DPH was used to replace NR.

Initial rate method: Initial rate experiments of various concentrations of C_8F_{17}-C_3H_6-TACN·Zn^{2+} and $C_{11}H_{23}$-TACN·Zn^{2+} to catalyze 200 μM HPNP to evaluate CACs were conducted in 10 mM HEPES buffer solution (pH 7.4) with a total volume of 3 mL, using UV–vis absorption spectrometer (UV-2600, Shimadzu, Japan) at 37 °C. For C_8F_{17}-C_3H_6-TACN·Cu^{2+} and $C_{11}H_{23}$-TACN·Cu^{2+} cases, the similar experimental procedures were conducted.

The measurement of CAC via adding HPNP of various concentrations:
10 μL 1 mM NR stock solution was added into 3 mL test tubes containing C_nF_{2n+1}-C_mH_{2m}-TACN·Zn^{2+} of various concentrations, HPNP of various concentrations, and 2 mL 10 mM HEPES buffer solution of pH 7.4 to obtain a series of solutions containing 10 μM NR. The solutions were kept at room temperature for 30 min and then used to record their fluorescence spectra. The excitation wavelength was set as 564 nm.

The catalysis experiments under the condition of fixed substrate concentration while increasing catalyst concentration:
Various concentrations of C_8F_{17}-C_3H_6-TACN·Zn^{2+}, $C_{11}H_{23}$-TACN·Zn^{2+}, C_8F_{17}-C_3H_6-TACN·Cu^{2+}, and $C_{11}H_{23}$-TACN·Cu^{2+} were used, respectively, to catalyze 200 μM HPNP to evaluate k_{obs} values through a time-scaning method in 10 mM HEPES buffer solution (pH 7.4) with a total volume of 3 mL, by using a UV–vis absorption spectrometer (UV-2600, Shimadzu, Japan) at 37 °C.

Morphology characterization:
TEM: The concentrations of C_nF_{2n+1}-C_mH_{2m}-TACN·Zn^{2+} stock solutions were set as their corresponding CACs. 3 μL of the C_nF_{2n+1}-C_mH_{2m}-TACN·Zn^{2+} assemblies or C_8F_{17}-C_3H_6-TACN·Cu^{2+} assemblies solution was dropped on ultra-thin carbon-supported copper mesh, respectively. Then, the samples were dried at room temperature to obtain TEM samples. Then, the morphologies were observed through a Transmission Electron Microscope (TEM, H-7650, Hitachi, Japan).

Laser scanning confocal microscope: 1 mL of the C_nF_{2n+1}-C_mH_{2m}-TACN·Zn^{2+} assemblies solution and 5 μL 1 mM NR solution were mixed, and then 5 μL mixed solution was dropped on a glass slide. The dropped glass slide was carefully covered by another glass slide, and the sample was place into the uploading sample position of a Laser scanning confocal microscope, and images were obtained from a Leica TCS SP8 instrument (Leica, Germany) equipped with a 552 nm laser for obtaining images.

EDTA replacement experiment:
(i) The scanning time-dependent Abs @ 400 nm of a tested solution containing 110 μM C_8F_{17}-C_3H_6-TACN·Zn^{2+}, 600 μM HPNP and 10 mM HEPES buffer (pH 7.4) were conducted at 37 °C by a UV-2600 spectrometer (Shimadzu, Japan), and for after a certain scanning time, then equimolar amount of EDTA and Zn^{2+} ions (110 μM) were added in turn into the tested solution to record the change of the curve of scanning time-dependent Abs @ 400 nm.
(ii) The scanning time-dependent Abs @ 400 nm of a tested solution containing 110 μM C_8F_{17}-C_3H_6-TACN·Zn^{2+}, 600 μM HPNP and 10 mM HEPES buffer (pH 7.4) were conducted at 37 °C by a UV-2600 spectrometer (Shimadzu, Japan), and for after a certain scanning time, three parts of 36.67 μM EDTA were added in turn for a certain scanning time interval to ensure the final added EDTA concentration equal to that of TACN·Zn^{2+}, and then 110 μM Zn^{2+} ion was added into the tested solution to record the change of the curve of scanning time-dependent-Abs @ 400 nm.

Control replacement experiment:
Similar to the procedure of above (i) section of “EDTA replacement experiment”, equimolar amount of 3-NA, 2-IA, and 1-BA, were used, respectively, to replace EDTA.

Catalyzing OPD oxidation experiment:
A certain volume of C_8F_{17}-C_3H_6-TACN stock solution and Cu^{2+} stock solution were added (the molar ratio was set as 1:1), respectively, to 1 mL of HEPES buffer solution (10 mM, pH of 7.4) containing 200 μM OPD to afford a final concentration of 90 μM (for C_8F_{17}-C_3H_6-TACN and Cu^{2+}). Immediately, the fluorescence spectra were measured with a certain time interval, in which 415 nm was used as the excitation wavelength.

Extraction cycle experiment:
After the time-dependent fluorescence spectra of the solution containing 90 μM C_8F_{17}-C_3H_6-TACN, 90 μM Cu^{2+}, and 200 μM OPD was scanned up to 3 h, this solution was taken to mix with an equal volume of perfluorohexane (1 mL). After shaking for 10 min, the upper “fluorous” phase was carefully separated and perfluorohexane was removed through a heated way by using a hairdryer. Then, another 1 mL of HEPES buffer solution (10 mM, pH of 7.4) containing 200 μM OPD were introduced, and the fluorescence spectral scanning was conducted again up to 3 h to finish one cycle. Other cycles were performed referred to the procedure of first cycle. For TEM measurement, after

perfluorohexane solvent was removed, 1 mL ultra-pure water was added to prepare TEM samples. The detailed procedure of TEM experiments was similar to above TEM section.

CGMD simulation calculations:

The coarse-grained models of the catalyst monomers $C_{11}H_{23}$-TACN·Zn^{2+} and C_8F_{17}-C_3H_6-TACN·Zn^{2+} and of the substrate (HPNP) were built by following the procedure for parameterization of any coarse-grained molecule as described in tutorials available from the official MARTINI Web site (http://cgmartini.nl). In this work, we used the recently published MARTINI 3.0 force field, which notably added new X-bead type for halogen compounds and D-bead type for divalent ions. The coarse-grained modeling procedure of each molecule was decomposed into four steps described below.

(1) All-atom model as reference: The initial three-dimensional structure of $C_{11}H_{23}$-TACN·Zn^{2+}, C_8F_{17}-C_3H_6-TACN·Zn^{2+} and HPNP were created with MarvinSketch 6.2.1 software from ChemAxon, then further edited by using UCSF Chimera 1.11.2 to add AM1-BCC atomic charges. The charge distribution between TACN moiety and Zn^{2+} ions was kindly provided by Dr. Adam Pecina at Institute of Organic Chemistry and Biochemistry of the CAS.[24] The python-based ACPYPE tool was used to generate the topology and parameter files for the generalized AMBER force field (GAFF). [25] Then, each molecule was placed into a cubic simulation box of size equal to the solute largest dimension plus twice 1.4 nm to avoid that the solute interacts with its virtual images caused by the periodic boundary conditions. The box was further filled with TIP3P water molecules. After minimizing its potential energy, each system was equilibrated with two 1 ns MD simulations, first in the NVT ensemble (constant Number of particles, Volume, and Temperature) by using the Berendsen coupling algorithm,[26] and then in the NPT ensemble (constant Number of particles, Pressure, and Temperature) by using the Nose-Hoover[27] and Parrinello-Rahman coupling methods.[28] Finally, the equilibrated system was submitted to a 20 ns production run in the same conditions as in the second equilibration step (T = 300 K and P = 1 bar), with the time constants τ_T = 0.5 ps and τ_P = 2.5 ps. In this work, all MD simulations were performed with the GROMACS 2019.1 software.[29] The electrostatic interactions were treated by using the smooth PME method[30] and the Lennard-Jones potentials were cut off at a distance of 1.2 nm. The length of all covalent bonds involving hydrogens was kept constant using the LINCS procedure, allowing a time step of 2 fs.

(2) From all-atom to coarse-grained model: The mapping of the three molecules from their all-atom models into coarse-grained ones was performed by following the MARTINI 3 mapping procedure [31] and are shown in Figures S17-S19.

(3) Coarse-grained bonded parameters: The coarse-grained bonded parameters were determined from the all-atom simulation as follows: First, the distances between the centers of mass of two chemically connected beads and the valence angles between two pseudo covalent bonds were calculated and analyzed by using the *gmx distance*, *gmx angle* and *gmx analyze* GROMACS tools. In parallel, a first coarse-grained model was built with a set of initial bonded parameters alongside with the non-bonded parameters extracted from the publicly available *martini_v3.0.3.itp* and *martini_v3.0_solvents.itp* files. Initial coarse-grained structures of each molecule were generated from the last frame of its all-atom simulation, and were further solvated in coarse-rained water. After a minimization of 10 000 steps, each coarse-grained system was first relaxed with a 250 ps simulation with a small time step of 5 fs, then equilibrated for 20 ns at T = 300 K and P = 1 bar by using the V-rescale temperature[32] and Parrinello-Rahman pressure[33] coupling methods with the constants τ_T = 1.0 ps and τ_P = 12.0 ps. All non-bonded interactions were cut off above a distance of 1.1 nm and the electrostatic ones were treated by using the reaction-field (RF) method with a relative dielectric constant ε_r = 15. The bond length and valence angle distributions of the coarse-grained trajectory were computed by using the same GROMACS tools as previously and further compared with those calculated from the all-atom simulation. The coarse-grained bonded parameters were then iteratively adjusted until the bond length and valence angle distributions satisfactorily match those of the all-atom model (Table S4-S6; Figures S17-S19). The obtained bonded parameters for HPNP, $C_{11}H_{23}$-TACN·Zn^{2+} and C_8F_{17}-C_3H_6-TACN·Zn^{2+} are reported in Tables S3-S5. In this coarse-grained model, all dihedral angles have energy barriers set to zero.

(4) Validation of coarse-grained model: To validate the coarse-grained model of catalyst monomer and substrate, the octanol-water partition free energy was considered and compared to experimental reference. However, considering that the experimental $logP_{ow}$ values for the whole catalyst have not been reported so far, only their building blocks (i.e., C_8F_{17} and C_2H_5-TACN·Zn^{2+}) were calculated in this work. The octanol-water partition coefficient P_{ow} is related to the octanol → water transfer free energy as: $logP_{ow} = \Delta G_{ow}/(2.303\ RT)$, with $\Delta G_{ow} = \Delta G_w - \Delta G_o$, where ΔG_w and ΔG_o are the solute solvation free energy in water and octanol respectively. T is the temperature and R is the molar gas constant (8.314 J/K/mol). In this work, the transfer free energy ΔG_{ow} was calculated by using the umbrella sampling (US) technique, in which a series of MD simulations were performed to pull the solute from the octanol bulk to the water bulk, by restraining the solute position along a reaction coordinate via harmonic bias potentials. The simulation conditions are the same as previously reported.[34] The final octanol-water transfer free energy ΔG_{ow} was estimated from the potential of mean force (or free energy profile) along the reaction coordinate extracted with the weighted histogram analysis method (Figure S20). The ΔG_{ow} and $logP_{ow}$ values of the catalyst components (C_8F_{17}-CH_3, C_2H_5-TACN·Zn^{2+}) and substrate (HPNP) calculated by this method are reported in Table S7 and compared with the theoretical values provided by the XLOGP3 program. The $logP_{ow}$ calculated from the coarse-grained models are in fair agreement with the XLOGP3 prediction. [35]

Coarse-grained MD simulation of self-assemblies:

The parameters of the molecule validated coarse-grained models were then used to set up systems composed of several chains as follows: First, an initial configuration was built by randomly placing 72 $C_{11}H_{23}$-TACN·Zn^{2+} or C_8F_{17}-C_3H_6-TACN·Zn^{2+} pro-catalyst monomers into a cubic box so that the solute concentration is 5 mM. After a minimization of 50 000

steps, the MARTINI non-polarizable water beads W were added to fill the box, and an appropriate number of them were replaced by sodium or chloride ions to reach the physiological concentration of 150 mM. The full system was minimized with 50 000 steps, then submitted to a 10 ns equilibration, and a 7 μs production run under the same conditions as the previous coarse-grained simulations (time step = 20 fs, T = 300 K, P = 1 bar, V-rescale and Parrinello−Rahman coupling times τ_T = 1.0 ps and τ_P = 12.0 ps, relative dielectric constant ε_r = 15, and nonbonded cutoff distance = 1.1 nm). Each $C_{11}H_{23}$-TACN·Zn^{2+} or C_8F_{17}-C_3H_6-TACN·Zn^{2+} pro-catalyst self-assemblies were simulated in the absence or in the presence of 72 HPNP substrate molecules into the same box as described above.

Trajectories were analyzed by using GROMACS tools. The pro-catalyst monomer aggregation process was monitored by calculating the number of aggregates and the number of chains in the largest aggregate as function of time by using *gmx clustsize* with a cut-off distance set to 0.5 nm. The aggregate diameter was calculated with *gmx gyrate*. The spatial location of each component in aggregates was quantified by the radial distribution function relative to the aggregate center by using *gmx rdf*. The contact number between pro-catalyst chains and substrates was calculated with *gmx mindist.*

Umbrella sampling simulation:

Umbrella sampling technique was employed to estimate the affinity of the substrate (HPNP) to the self-assembled $C_{11}H_{23}$-TACN·Zn^{2+} or C_8F_{17}-C_3H_6-TACN·Zn^{2+} catalyst systems by calculating their corresponding binding free energy (ΔG_{bind}).[36] A previously formed catalyst-substrate micelle was extracted and placed in a rectangular box at 14 × 14 × 28 nm. The system was firstly minimized with 5000 steps, then equilibrated for 20 ns at T = 300 K and P = 1 bar by using the V-rescale temperature and Parrinello-Rahman pressure coupling methods (in the same condition as those used in previous CG-MD simulations). A randomly selected single HPNP molecule was pulled out from the self-assembled catalyst-substrate systems to the aqueous phase over 80 000 ps by using a harmonic force constant of 500 kJ/mol/nm^2 and a pulling rate of 0.005 nm/ps between the selected HPNP and the center of mass of the micelle to generate a series of initial configurations along a ξ axis coordinate. Then each configuration (or window) of the system was shortly equilibrated during 20 ns and then submitted to a 50 ns production run. The free energy profile of the solute along the ξ axis, also referred to as potential of mean force, is extracted from all simulations by using the weighted histogram analysis method (WHAM) implemented in the GROMACS utility *gmx wham*. The free energy profiles were used to calculate the binding free energy ΔG_{bind}.

Supporting Information

Synthesis and characterization of TACN derivatives and substrate HPNP, Supplementary experimental results, and NMR and MS spectra of TACN derivatives and HPNP (Figures S21-S53).

The authors have cited additional references within the Supporting Information.[S1-S4]

Acknowledgements

This work was supported by the Fujian Provincial Department of Science and Technology (No. 2020Y0038), the Xiamen Municipal Bureau of Science and Technology (No. 3502Z20193029), and Ningde Normal University (No. FJKL_FBCM202106), also supported by Xiamen Key Laboratory of Optoelectronic Materials and Advanced Manufacturing (Huaqiao University).

Keywords: polyfluoroalkyl chain • supramolecular catalysis • catalysis modulation • catalysis diversity • robust assemblies

[1] (a) J. F. Shi, Y. Z. Wu, S. H. Zhang, Y. Tian, D. Yang, Z. Y. Jiang. *Chem. Soc. Rev.* **2018**, *47*, 4295-4313. (b) Y. H. Lin, J. S. Ren, X. G. Qu. *Acc. Chem. Res.* **2014**, *47*, 1097-1105.

[2] (a) S. Y. Liu, P. D. Du, H. Sun, H. Y. Yu, Z. G. Wang. *ACS Catal.* **2020**, *10*, 14937-14958. (b) J. J. Han, Q. L. Zou, Su, W. W., Yan. X. H. *Chem. Eng. J.* **2020**, *394*, 124987. (c) M. D. Nothling, Z. Y. Xiao, A. Bhaskaran, M. T. Blyth, C. W. Bennett, M. L. Coote, L. A. Connal. *ACS Catal.* **2019**, *9*, 168-187.

[3] (a) Z. G. Wang, Y. Z. Li, H. Wang, K. W. Wan, Q. Liu, X. H. Shi, B. Q. Ding. *Chem. Eur. J.* **2019**, *25*, 12576-12582. (b) C. Q. Zhang, X. D. Xue, Q. Luo, Y. W. Li, K. N. Yang, X. X. Zhuang, Y. G. Jiang, J. C. Zhang, J. Q. Liu, G. Z. Zou, X. J. Liang. *ACS Nano* **2014**, *8*, 11715-11723.

[4] (a) P. S. MuÇana, G. Ragazzon, J. Dupont, C, Z.-J. Ren, L. J. Prins, J. L.-Y. Chen. *Angew. Chem.* **2018**, *57*, 16469-16474. (b) F. Mancin, L. J. Prins, P. Pengo, L. Pasquato, P. Tecilla, P. Scrimin. *Molecules* **2016**, *21*, 1014-1032.

[5] (a) D. Zaramella, P. Scrimin, L. J. Prins. *J. Am. Chem. Soc.* **2012**, *134*, 8396-8399. (b) R. Bonomi, A. Cazzolaro, A. Sansone, P. Scrimin, L. J. Prins., *Angew. Chem.* **2011**, *50*, 2307-2312.

[6] Y. J. Cao, M. X. Yao, L. J. Prins, R. X. Ji, N. Liu, X. Y. Sun, Y. B. Jiang, J. S. Shen. *Chem. Eur. J.* **2021**, *27*, 7646-7650.

[7] B. Gruber, E. Kataev, J. Aschenbrenner, S. Stadlbauer, B. König. *J. Am. Chem. Soc.* **2011**, *133*, 20704-20707.

[8] C. Z.-J. Ren, P. Solís-Muñana, G. G. Warr, J. L.-Y. Chen. *ACS Catal.* **2020**, *10*, 8395-8401.

[9] R. A. Moss, K. G. Ragunathan. *Langmuir* **1999**, *15*, 107-110.

[10] C. A. Bunton, P. Scrimin, P. Tecilla. *J. Chem. Soc., Perkin Trans. 2.* **1996**, *3*, 419-425.

[11] F. Mancin, P. Scrimin, P. Tecilla, U. Tonellato. *Coord. Chem. Rev.* **2009**, *253*, 2150-2165.

[12] F. M. Menger. *C. R. Chim.* **2009**, *12*, 54-60.

[13] (a) Klotz, I. M. Enzyme Mechanisms (Eds.: M. I. Page, A. Williams), Royal Society of Chemistry, London, **1987**, chap. 2. (b) J. Suh. *Acc. Chem. Res.* **2003**, *36*, 562-570. (c) F. Mancin, P. Scrimin, P. Tecilla, U. Tonellato. *Coord. Chem. Rev.* **2009**, *253*, 2150-2165.

[14] M. P. Krafft, J. G. Riess. *Chem. Rev.* **2009**, *109*, 1714-1792.

[15] C. Gentilini, F. Evangelista, P. Rudolf, P. Franchi, M. Lucarini, L. Pasquato. *J. Am. Chem. Soc.* **2008**, *130*, 15678-15682.

[16] O. Iranzo, T. Elmer, J. P. Richard, J. R. Morrow. *Inorg. Chem.* **2003**, *42*, 7737-7746.

[17] S. Uchida, S. Hikichi, T. Akatsuka, T. Tanaka, R. Kawamoto, A. Lesbani, Y. Nakagawa, K. Uehara, N. Mizuno. *Chem. Mater.* **2007**, *19*, 4694-4701.

[18] G. Absillis, E. Cartuyvels, R. V. Deun, T. N. Parac-Vogt. *J. Am. Chem. Soc.* **2008**, *130*, 17400-17408.

[19] S. G. Kleemann, W. M. Keung, J. F. Riordan. *J. Inorg. Biochem.* **1986**, *26*, 93-106.

[20] K. M. Hendrickson, J. P. Geue, O. Wyness, S. F. Lincoln, A. D. Ward. *J. Am. Chem. Soc.* **2003**, *125*, 3889-3895.

[21] C. A. Hunter, H. L. Anderson. *Angew. Chem.* **2009**, *48*, 7488-7499.

[22] J. S. Shen, J. J. Wu, X. Y. Sun, Z. L. Wu, P. Gao, B. Liu. *J. Mater. Chem. C* **2017**, *15*, 3757-3764.
[23] Z. Han, D. Y. Nan, H. Yang, Q. Q. Sun, S. Pan, H. Liu, X. L. Hu. *Sensor Actuat B-Chem* **2019**, *298*, 126842.
[24] A. Pecina, D. Rosa-Gastaldo, L. Riccardi, S. Franco-Ulloa, E. Milan, P. Scrimin. *ACS Catal.* **2021**, *11*, 8736-8748.
[25] J. M. Wang, R. M. Wolf, J. W. Caldwell, P. A. Kollman, D. A. Case. *J. Comput. Chem.* **2004**, *25*, 1157-1174.
[26] U. Bren, C. J. Oostenbrink. *Chem. Inf. Model.* **2012**, *52*, 6, 1573-1582.
[27] (a) S. A. Nosé. *J. Chem. Phys.* **1984**, *81*, 511-519. (b) W. G. Hoover. *Phys. Rev. A: At., Mol., Opt. Phys.* **1985**, *31*, 1695-1697.
[28] M. Parrinello, A. J. Rahman. *Appl. Phys.* **1981**, *52*, 7182-7190.
[29] M. J. Abraham, T. Murtola, R. Schulz, S. Páll, J. C. Smith, B. Hess, E. Lindahl. **2015**, SoftwareX, 1-2, 19-25.
[30] U. Essmann, L. Perera, M. L. Berkowitz, T. Darden, H. L. Lee, G. J. Pedersen. *Chem. Phys.* **1995**, *103*, 8577-8593.
[31] (a) S. J. Marrink, H. J. Risselada, S. Yefimov, D. P. Tieleman, A. H. de Vries. *J. Phys. Chem. B* **2007**,*111*,7812-7824. (b) R. Alessandri, J. Barnoud, A. S. Gertsen, I. Patmanidis, A. H. de Vries, P. C. T. Souza, S. J. Marrink. *Adv. Theory Simul.* **2022**, *5*, 2100391.
[32] G. Bussi, D. Donadio, M. J. Parrinello. *Chem. Phys.* **2007**, *126*, 014101.
[33] M. Parrinello, A. Rahman. *J. Appl. Phys.* **1981**, *52*, 7182-7190.
[34] P. Gao, J. Nicolas, T. Ha-Duong. *J. Am. Chem. Soc.* **2021**, *143*, 17412-17423.
[35] T. Cheng, Y. Zhao, X. Li, F. Lin, Y. Xu, X. Zhang, Y. Li, R. Wang, L. J. Lai. *Chem. Inf. Model.* **2007**, *47*, 2140-2148.
[36] (a) Lemkul J, A., Bevan, D. R. *J. Phys. Chem. B* **2010**, *114*, 1652-1660. (b) T. Duran, A. Costa, A. Gupta, X. M. Xu, H. L. Zhang, D. Burgess, B. Chaudhuri. *Mol. Pharmaceut.* **2022**, *19*, 1117-1134.

Entry for the Table of Contents

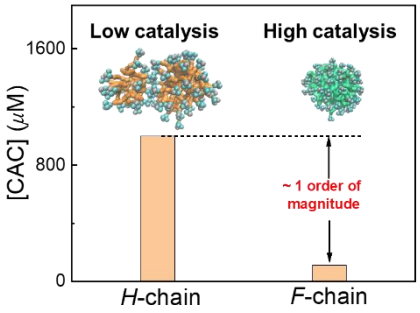

Polyfluoroalkyl chain-based TACN derivatives were developed to lower their CAC in the presence of equimolar amount of Zn^{2+} ions to drive the self-assembly and afford high catalytic activity towards the hydrolysis reaction of HPNP, demonstrating the robustness of *F*-chain assemblies, compared with their perhydroalkyl chain counterparts.